



**HAL**  
open science

# Design and experimental analysis of a high force piezoelectric linear motor

Sofiane Ghenna, Yves Bernard, Laurent Daniel

► **To cite this version:**

Sofiane Ghenna, Yves Bernard, Laurent Daniel. Design and experimental analysis of a high force piezoelectric linear motor. *Mechatronics*, 2023, 89, pp.102928. 10.1016/j.mechatronics.2022.102928 . hal-03882445

**HAL Id: hal-03882445**

**<https://hal.science/hal-03882445>**

Submitted on 23 Jun 2023

**HAL** is a multi-disciplinary open access archive for the deposit and dissemination of scientific research documents, whether they are published or not. The documents may come from teaching and research institutions in France or abroad, or from public or private research centers.

L'archive ouverte pluridisciplinaire **HAL**, est destinée au dépôt et à la diffusion de documents scientifiques de niveau recherche, publiés ou non, émanant des établissements d'enseignement et de recherche français ou étrangers, des laboratoires publics ou privés.

# Design and experimental analysis of a high force piezoelectric linear motor

Sofiane Ghenna<sup>a,b,c,\*</sup>, Yves Bernard<sup>a,b</sup>, Laurent Daniel<sup>a,b</sup>

<sup>a</sup>Université Paris-Saclay, CentraleSupélec, CNRS, Laboratoire de Génie Electrique et Electronique de Paris, 91192, Gif-sur-Yvette, France.

<sup>b</sup>Sorbonne Université, CNRS, Laboratoire de Génie Electrique et Electronique de Paris, 75252, Paris, France.

<sup>c</sup>Univ. Polytechnique Hauts-de-France, CNRS, Univ. Lille, Yncrea, Centrale Lille, UMR 8520 - IEMN, F-59313 Valenciennes, France.

## Abstract

In this paper, the design and experimental analysis of a piezo-motor for applications requiring compact size, high blocking and driving forces are presented. Mechanical design addresses difficulties associated with high integration flexibility and high blocking force for the motor. The technology is inspired from a real inchworm motion and is based on Piezoelectric Actuators (PAs). The proposed Inchworm Motor (IM) consists of an extending mechanism (EM) and two doubled clamping mechanisms (CMs). Theoretically and by using Finite Element Analysis (FEA), the CM is designed in order to obtain high clamping forces between rotor and stator (2500 N), while the EM is designed for large displacement (free stroke of 0.01 mm) and high force (500 N) using PAs. Practically and by using a preliminary low power supply (80 V, 1 Hz), the working principle of the motor is validated under testing conditions of 300 N as a clamping force and 5 N as a driving force. The fabricated IM achieves speed of  $2.25 \mu\text{m s}^{-1}$ . Experimental methods for verifying the theoretical force, calibrating the pre-stressing force and measuring the friction coefficient between the stator and the rotor are proposed. A motor with a weight of 78 g and dimensions of  $100 \text{ mm} \times 16 \text{ mm} \times 7 \text{ mm}$  ensures full clamping ability when not electrically activated.

**Keywords:** Inchworm motor, Linear motor, Clamping Mechanism, Finite Element Analysis, Actuator, Friction.

## 1. Introduction

Conventional electromagnetic linear motors are essentially rotating electrical machines which have been coupled to a transformation motion system in order to provide linear motion. This conventional solution requires a large volume and also needs a motion transformation system. On the other hand, linear electromagnetic motors can produce directly a linear motion, but their clamping ability is still an important issue when they are not electrically activated. Moreover, these electromagnetic actuators need a number of add-on components, for example a driver circuit with precise position sensing systems. Currently, actuators based on smart materials can offer more advantages over traditional motors, including higher accuracy and power density, less maintenance and less noise. They are simpler and require a smaller installation. Among these actuators, piezoelectric actuators are promising solutions, they have a fast transient response characteristics, high blocking force capability, small size, and high electromechanical coupling efficiency. In this paper, a Piezoelectric Actuator (PA) system providing directly a linear motion with high clamping and driving force is developed. The idea is to provide a compact PA system with full clamping ability when not activated. An inchworm<sup>1</sup> type piezoelectric motor is chosen. A piezoelectric Inchworm Mo-

tor (IM) is inspired from the motion features of natural inchworm. Since they have no legs in the middle portion of their body, inchworms need to pull their hind portion forward forming a loop, and then move forward with the front portion of their body. The movement of an IM proceeds from an analogy with the locomotion mode of inchworms. The motor can achieve a long range motion by repeating a clamp-extend-clamp pattern (the motions consist of clamping motions and extension / contraction motions). They typically use parallel guide rails, two PAs for two Clamping Mechanisms (CMs) and a third for the Extending Mechanism (EM), as shown in Fig 1. In this configuration, the parallel guide rails are fixed (stator) with respect to moving parts A, B and C (rotor). IM has drawn much atten-

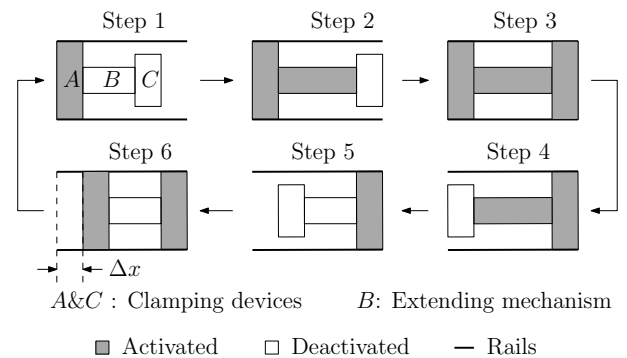


Figure 1: Basic actuation sequence of a piezoelectric IM with full clamping when electrically activated

tion especially for high precision positioning devices [1, 5, 8]

\*Corresponding author

Email addresses: sofiane.ghenna@uphf.fr (Sofiane Ghenna),

yves.bernard@centralesupelec.fr (Yves Bernard),

laurent.daniel@centralesupelec.fr (Laurent Daniel)

<sup>1</sup>Inchworm is a registered trademark of Burleigh Instruments, Inc.

because of its compact size, flexible design, and very simple mechanical structure that does not need any electromagnetic fields. Even though it can provide high accuracy, high speed, less noise and clean environment, however, their load capability in terms of clamping force (contact forces between rotor and stator) and driving force are usually limited as one can find out by the comparison between the different IM performances reported in Tab.1. The operating characteristic of piezoelectric linear actuator based motor has been investigated in several works as reported Tab.1, and the clamping force of inchworm linear motors is still limited. It should be noted that the clamping force should be higher than the driving force. In order to enlarge the clamping force range, excitation voltage amplitude, volume and weight of CMs (more space for PAs) can be increased. The maximum clamping force was obtained by [3] with a volume of  $16.85 \text{ cm}^3$  and a voltage of 200 V. The maximum driving force was obtained recently by [25] with a large volume compared to [3]. The IM reported in [8] has the same blocking force as [2] with half its volume. However, in order to achieve this level of clamping force, the IM presented in [8] was excited with 450 V. On the other hand, since the displacements of PAs are usually in the range of a few tens of micrometers, the matching accuracy must be in the same range to ensure full clamping force for both clamps. In order to increase the speed of IMs, other configurations [14, 17, 18, 19] refer to resonant type longitudinal vibration transducers. For example, in [14], a cosine voltage is applied on both transducers in the CM, while a sine voltage is applied to the transducer in the EM. The first longitudinal vibrations of transducers are superimposed to produce elliptical motion between the clamps and rails (see Fig.1). Even though the configuration reported in [20] can operate in both quasi-static and resonant modes, its driving force is limited to 0.5 N. The majority of IMs are designed with 3 piezo actuators except works reported in [23] based on a linear walking stage and in [15] based on double-foot piezoelectric linear motor or by using double stators [16]. The speed of these IMs depends on the switching frequency of the driving signal and voltage amplitude. The IM speed will increase at a higher frequency of operation without modifying the weight and volume of the motor.

In this paper, a trade-off between increasing the load capacity and reducing the inchworm weight and volume has been investigated. In addition the CMs ensure full clamping when not activated in contrast to the configurations reported in [1, 2], [4, 6, 7, 9] and [11, 12, 13, 15, 24, 26, 27] where an electrical excitation is needed in order to ensure the clamping ability as reported in a recent works [28, 29]. In this work, two blocks on both CMs are adopted in order to support high blocking force with self-locking at power off. Locking between rotor and stator is naturally provided with the absence of electrical excitation. Hence, in the CMs, the actuators are electrically excited only to unlock the rotor from the stator. The proposed motor is designed for a free stroke of 0.01 mm. Hence, the speed of the motor is  $0.01 \text{ mm s}^{-1}$  for an excitation frequency of 1 Hz. This speed can be increased by increasing the excitation frequency. The high challenge that reported in this work is linked to development of compact piezoelectric system with high perfor-

mances, including dimensions of  $100 \text{ mm} \times 16 \text{ mm} \times 7 \text{ mm}$  and a weight of 78 g. In this work, the proposed IM can be used to actuate aero plane pilot seats where low weight and large forces are required. It can be also used for linear translation applications such as micro-manipulation for micro positioning field. This paper is organized as follows. In the first part, the IM design is presented, with its operating principle and an analysis of the EM. Then, a FEA analysis of the CM and the EM using COMSOL Multiphysics® with PA selection is detailed. The experimental validation is introduced in the second part including PAs test off load, calibration of the pre-stressing force, EM and CMs displacement measurement with blocking force measurement. Finally, motor speed, load and frequency influence are presented.

## 2. Inchworm Motor design

The objective of this work is to develop an IM for applications requiring high blocking and driving force. In addition, the IM must ensure full clamping ability when not activated (self-locking at power off) which is an essential pre-requisite for several industrial applications especially for low power consumption. Features of the developed IM include small weight ( $< 100 \text{ g}$ ) and small size ( $< 11.5 \text{ cm}^3$ ).

### 2.1. Proposed Linear motor

The proposed IM design is given in Fig.2(a). By analogy to an inchworm, this motor contains a rotor (moving part) which includes two CMs and an extender. Five PAs are implemented in the IM and EM, which pre-tightening elements consist of two pre-tightening blocks and screw in order to offer a mechanical protection for PAs. The connection between CM and EM is provided by screw and nut junction. Two double pairs of clamp were considered in order to withstand high blocking forces. Consequently, a pair of PAs for each clamp is installed. To ensure the function of the IM, a stator has been designed in such a way that it provides on one hand a guide for the rotor and on the other hand to apply a blocking force<sup>2</sup> on CMs. Stator is divided into two parallel rails. One is integrated with the base of the rotor and is considered fixed, while the second is moving according to Y-axis. In order to maintain a uniform and constant blocking force on the rotor, screws have been used as indicated in Fig.2(b).

In this work, the stator is considered rigid and it is assumed that there is no gap between rotor and stator. Moreover, non-linearity in the PA system is neglected.

In order to ensure full clamping ability when the linear motor is not electrically activated, the rotor is initially blocked through stator (mechanically). Here, the PAs are placed along X-Axis. When the PAs are activated, the horizontal motion (along X-Axis) of CM is transformed into a vertical motion (along Y-Axis), then the CM is unlocked. CM dimensions were chosen in such a way that the vertical force is amplified. This configuration naturally ensures self-locking at rest. When the PAs are

<sup>2</sup>Tangential friction forces between stator and rotor according to X-Axis

Table 1: Performance of various IMs

References	Clamping force [N]	Driving force [N]	Velocity [mm s <sup>-1</sup> ]	Actuation frequency [Hz]	Voltage [V]	Volume [cm <sup>3</sup> ]	Numbers of PAs [unit]
1994, [1]	-	200	1.6	-	-	-	3
1999, [2]	200	41.5	6	1000	124	48	3
2001, [3]	450	50	11	30	200	16.85	3
2002, [4]	-	170	5	50	130	-	3
2003, [5]	-	-	0.0013	15	100	-	3
2004, [6]	-	20	5	500	-	-	3
2004, [7]	-	70	2.7	320	100	101	3
2005, [8]	200	100	50	2000	450	25.28	3
2005, [9]	55	-	-	-	200	-	3
2006, [10]	-	10	20	-	-	-	3
2007, [11]	-	6	8.5	800	200	-	3
2013, [12]	21	10	2	70	150	-	3
2013, [13]	-	39	1.14	30	180	-	3
2016, [14]	-	158.2	800	33150	250	265	3
2017, [15]	-	10	4	110	100	-	4
2018, [17]	-	1.17	1641	41470	250	32.7	3
2019, [18]	-	70	1.075	150	150	296	3
2020, [21]	-	8	209	22700	100	30.8	3
2020, [22]	-	3.28	0.72	50	120	202.5	3
2021, [23]	-	4.9	0.028	30	200	169	2
2021, [24]	-	1.2	1.54	120	150	432	3
2022, [25]	-	546	0.043	250	120	112	3

turned off, the rotor is blocked. The PA in the EM is the source of the driving force. This design is devoid of motion converter system (rotary to linear motion).

## 2.2. Operating principle

The operating principle of this motor is presented in Fig.3. Operation cycle consists of six steps divided in two phases as described in Fig.3(a). These phases produce an axial displacement. The motor ensures full clamping ability when not activated. At the beginning (step (f)) the clamping actuators are not excited, then clamp (A) and (B) are closed (in contact with the stator). In the first phase (a, b and c), when the input current for the clamp (A) actuator is turned on (step (a)), the clamp (A) releases (gap between rotor and stator). Then, the extending actuator is activated and the EM extends (step (b)). Consequently, the first half part of the motor is moving before closing clamp (A) in step (c). In the second phase (d, e and f), after the clamping changes from (A) to (B) (step (d)) and the extending actuator is turned off (step (e)), the extender contracts to its original position. Consequently, the second half part of the motor is moving before closing clamp (B) (step (f)) and so on. For most of IMs, three input signals are needed, one for the driving unit (extender) and the other two for the clamping unit as shown in Fig.3(b). The direction of motion can also be changed through changing the driving signal sequence of the PAs of CM (A) and (B). The speed of the IM depends on the excitation frequency and voltage amplitude of the PA in the extender [30].

## 2.3. Analysis of the CM

The CM determines the limitation of the IM in terms of blocking force which influences the maximum produced driving force. For the proposed application requiring high blocking force, an amplified piezoelectric actuator is required as given in Fig.4. This mechanism looks like an hexagon that contracts vertically as the fitted PA expands horizontally. This part gives an idea about the angle of the oblique beams  $\phi$  to amplify or reduce (force /displacement) before investigating the thickness, width or material of the clamps. Similar geometrical structure has already been developed by Cedrat-technologies [31]. According to the structure dimensions, the horizontal motion (along X-Axis) is transformed into a vertical motion (along Y-Axis), and the output displacement (vertical displacement) is amplified or reduced. By analogy to the displacement the driving force is reduced or amplified. The displacement amplification gain  $G$  is given by Eq.1

$$G = \frac{\Delta y}{\Delta x} \quad (1)$$

According to Fig.4, the final vertical position  $y_1$  is

$$y_1 = \sqrt{y_0^2 - [(\Delta x^2) + 2\Delta x(x_0 - b)]} \quad (2)$$

Eq.2 can be expressed as follows:

$$\Delta y(y_0 + y_1) = \Delta x[\Delta x + 2(x_0 - b)] \quad (3)$$

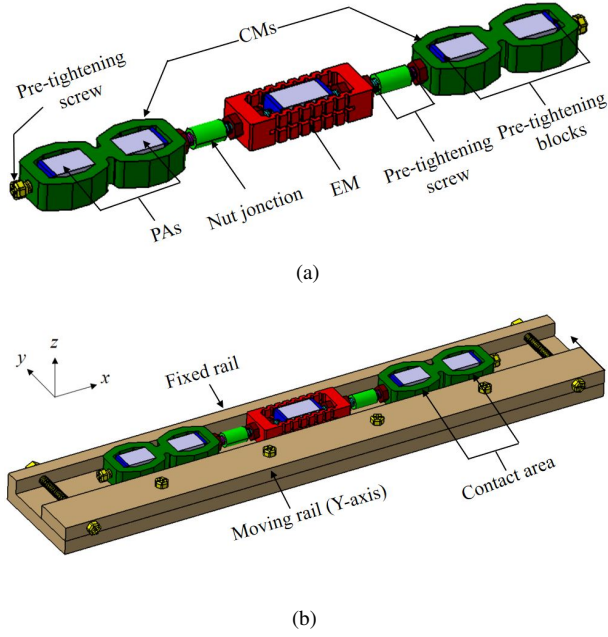


Figure 2: Proposed IM design with self-locking at rest, (a) rotor, (b) rotor and stator

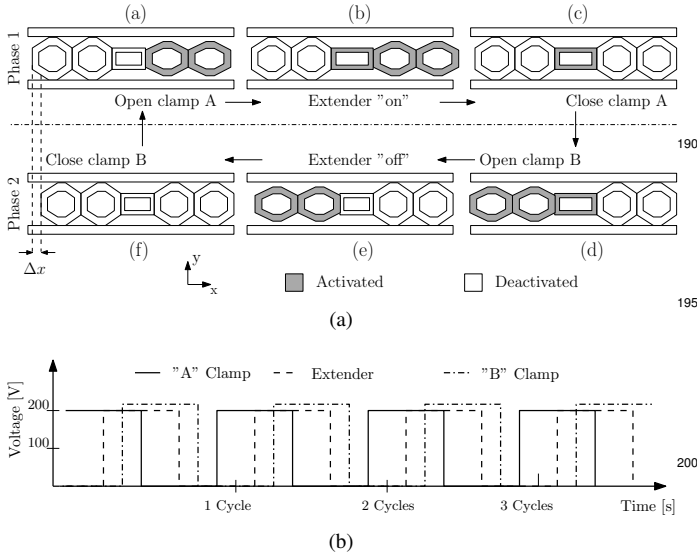


Figure 3: Operating principle, (a) Six actuations result in one step motion with full clamping ability when not electrically activated, (b) Driving signal sequence during three cycles at a given frequency

From Eq.1 and 3 under assumption of small  $\Delta x$  ( $\Delta x \ll 2y_0$  and  $y_1 + y_0 \approx 2y_0$ ), the amplification can be expressed as follows

$$G \approx \frac{x_0 - b}{y_0} = \cot \phi \quad (4)$$

According to Eq.4 the vertical displacement is amplified if the angle of the oblique beams  $\phi$  is less than  $\frac{\pi}{4}$ . This instantaneous amplification gain does not apply to large displacement because of the nonlinearity in Eq.2

In this work, the proposed CM reported in Fig.2(a) is based on a double amplified piezoelectric actuator in order to support high

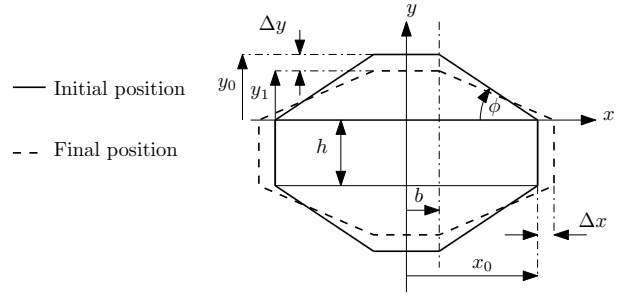


Figure 4: Motion sequence during three cycles

blocking force.

### 3. FEA Analysis

3D FEA was conducted using COMSOL Multiphysics® to gain insight into device operation, and to determine the performance of the IM.

#### 3.1. Clamping Mechanisms

The CMs should produce a high frictional force with rails. On the other hand, CMs should support the static force of the load and the dynamic force of the EM. For this reason the configuration given in Fig.2 was adopted. This clamp naturally ensures the amplification of the applied force by PAs in order to release the rotor from stator. Moreover, deformation and stress depend on geometry as well as material properties. In order to achieve appropriate stiffness for the clamp, length, width and thickness have been varied under COMSOL Multiphysics®. The characteristics of the material that will be used in the design of the IM are very important. First we need a very rigid material to support the forces to be imposed without exceeding the limit of elasticity of the constitutive material. In fact, a hard material allows us to obtain a high stiffness. In comparison with another material with a lower stiffness, for a given force, the displacement will be lower, therefore the length of the piezoelectric actuators to be used will be shorter, which is more beneficial from several points of view: volume, weight, and cost. Another important point is the possibility of obtaining a high coefficient of friction to favor the clamping force. For this reason the selected material was steel with a density of  $7860 \text{ kg/m}^3$ , elastic modulus of  $200 \text{ GPa}$ , and Poisson ratio of  $0.266$ .

In order to achieve the performances of the proposed IM given in Tab.1 (clamping force and volume), the final dimensions of the clamp are indicated in Fig.5. The contact area between clamp and stator is considered perfect and is modelled using penalty method in COMSOL Multiphysics®.

##### 3.1.1. Clamp closure

The objective here is to obtain a high clamping force, then a high friction coefficient between the stator and rotor is required. In this paper, it is supposed that the friction coefficient is equal to 1 according to the chosen material. Hence, the tangential frictional force is equal to contact normal force. Since a perfectly fixed and rigid rail was considered, it is possible to

take into account four contact surfaces between clamp and stator (see Fig.2(a)). For a clamp closure, as a load conditions, we have applied a preloading force by the stator (rails). It applies a normal force on the clamp through the contact area, and induces a tangential frictional force between stator and clamp (X-axis). The integrated rail with the base of the rotor (clamp) is considered fixed, while the second is moving according to Y-axis. The clamp (rotor) is also considered fixed and then a contact force is obtained by considering a pair of contact between the two rails and fixed clamp.

### 3.1.2. Clamp aperture

A static structural analysis is carried out and a contact force (rotor/stator) of 1250 N for one clamp is obtained (312 N for each contact surface) according to subsection 3.1.1 . The clamp aperture criterion consists of zero contact force between rotor and stator. The Von-Mises stress obtained by FEA is shown in Fig.5. It is possible to show that the force of two PA ( $2 \times 640$  N)

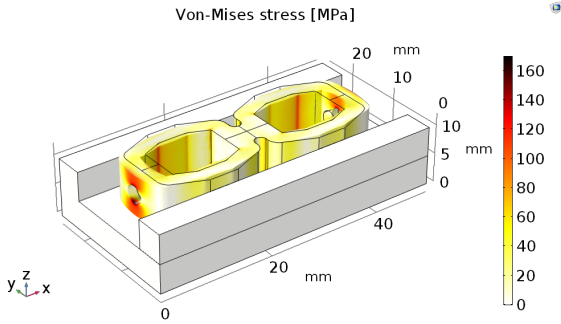


Figure 5: Von-Mises stress of clamp aperture (3D view)

is enough to obtain zero contact force. The contraction can be ensured only if the simulated stress is lower than the limit of elasticity of the chosen constitutive material (250 MPa) as confirmed by the figure (180 MPa). The resulting VM stress in the rail is zero MPa (no contact). Fig.6 shows simulation results of displacement distribution in response to two PA forces of 640 N along X-axis and Y-axis. When one of the clamps is blocked on the stator, a displacement of  $7 \mu\text{m}$  along X-axis induces a displacement of  $3.5 \mu\text{m}$  along Y-axis. As a result, a contact force of 0 N is obtained (no contact). The stiffness of the CM is  $91 \text{ N} \mu\text{m}^{-1}$ .

### 3.2. Extending mechanism

The EM controls the speed and the driving force of the motor. This device has been designed in order to provide a driving force of 500 N. PAs do not offer a practical mechanical interface for a direct contact and connection between the two CMs. Hence, the implementation of PA into a metal casing improves reliability. Moreover, it protects the PA from mechanical impact and external environmental factor. For this reason, a pre-tightening part shown in Fig.2(a) is proposed. Here, the design criteria is based on the elasticity of the extender, its height and width which should not exceed the those of the clamping mechanism. This extender acts as a spring when the PA is turned on.

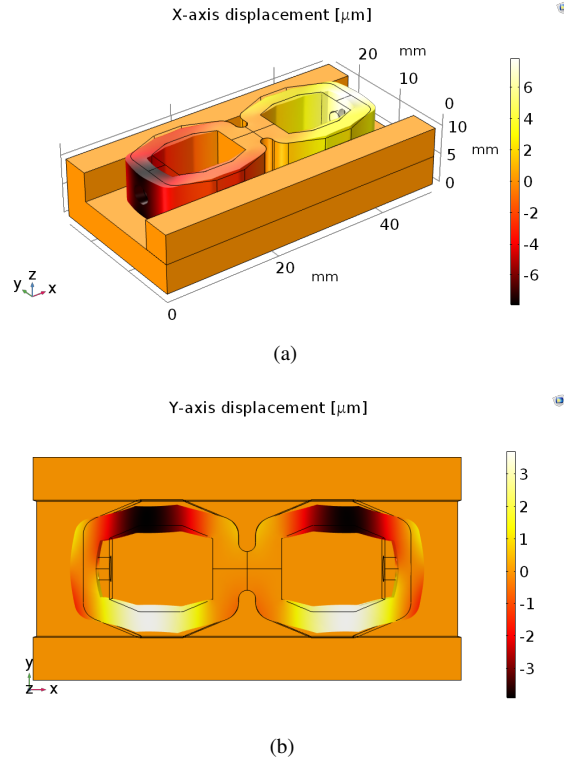


Figure 6: Clamp displacement distribution in the extending mode along, (a) X-axis (3D view ) and (b) Y-axis (top view)

#### 3.2.1. Extending and retracting mode

A PA force of 500 N was applied on the elastic actuator along X-axis, as a result a displacement stroke of  $13 \mu\text{m}$  was obtained as shown in Fig.7, meaning that the stiffness of the extender is  $38 \text{ N} \mu\text{m}^{-1}$ . When the PA in the extending mechanism

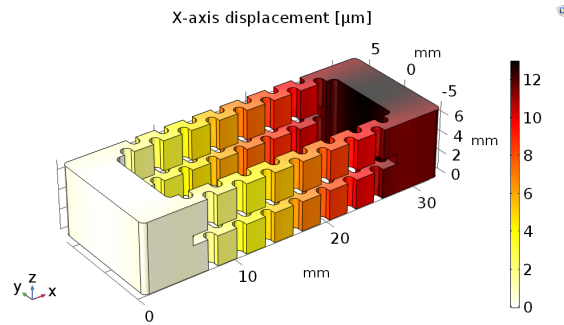


Figure 7: Extender displacement distribution in the extending mode along X-axis (3D view)

is turned off, the extender retracts. Provided that the maximum Von-Mises stress is lower than the yield stress of the constitutive material (250 MPa), the retracting mode is ensured, as shown in Fig.8. Knowing the stiffness of the inchworm mechanical structure, it is possible to select the required PA in terms of generated force, displacement and dimensions.

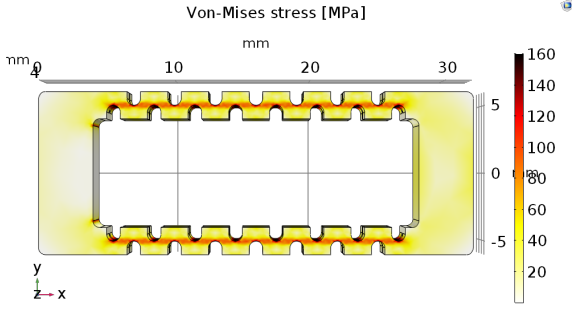


Figure 8: Extender Von-Mises stress in the extending mode (top view)

Table 2: Noliac Piezo-actuator characteristics

Type	Dimensions [mm <sup>3</sup> ]	Free stroke [ $\mu\text{m}$ ]	Blocking force [N]
NAC2021-H10	7x7x10	13.2	2060
NAC2021-H16	7x7x16	23.1	2060

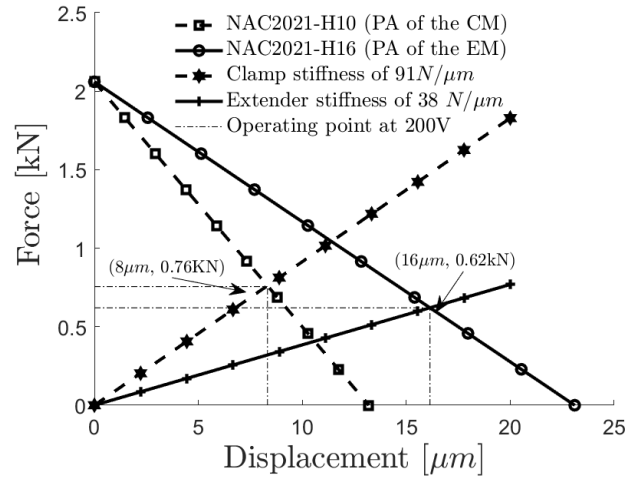


Figure 9: Theoretically force vs displacement output of Noliac PAs  $\pm 15\%$  of the CM and the EM at 200V, and simulated stiffness of the CM and EM

#### 4. PA characteristics in CM and EM

PA selection is a critical issue, because the actuator force generation is always coupled with a reduction in displacement. Hence, the stiffness of the inchworm mechanical structure should be intersecting with the PAs force/displacement curves. From Fig.6, the total required displacement in order to open the clamp is  $7\mu\text{m}$  with a force of 640 N, i.e. a stiffness of  $91\text{ N}\mu\text{m}^{-1}$ , while the stiffness of the EM is  $38\text{ N}\mu\text{m}^{-1}$ . PAs with stiffness identical to the stiffness of CM and EM are required. Regarding dimensions of the CM and EM, PAs with cross section of  $7\text{ mm} \times 7\text{ mm}$  and length of 10 mm and 16 mm, are the most economical choice for the CM and EM respectively. The characteristics of the chosen PAs are given in Tab.2. The PA maximum operating voltage is 200 V. These data are given with tolerance of  $\pm 15\%$ . The nominal operating points at operating voltage of 200 V are presented in Fig.9. The first one is the the intersection between the lines NAC2021-H10 and clamp stiffness. While the second one, is the intersection between lines NAC2021-H16 and extender stiffness.

#### 5. Experimental validation

A prototype with dimensions of  $100\text{ mm} \times 16\text{ mm} \times 7\text{ mm}$  was manufactured. All parts of the IM were made of steel and machined independently as shown in Fig.10. The chosen tolerance was  $\pm 0.1\text{ mm}$  as a first step. The contact surfaces was machined to nearly smooth finish, with Roughness<sup>305</sup> average  $R_a$ <sup>3</sup> of  $0.8\mu\text{m}$ . This  $R_a$  allows a freedom of movement with only a few microns normal displacement of the CM.

<sup>3</sup>Arithmetic average of the absolute values of the profile height deviations<sup>310</sup> from the mean line,  $R_a = \frac{1}{l} \int_0^l |y(x)| dx$

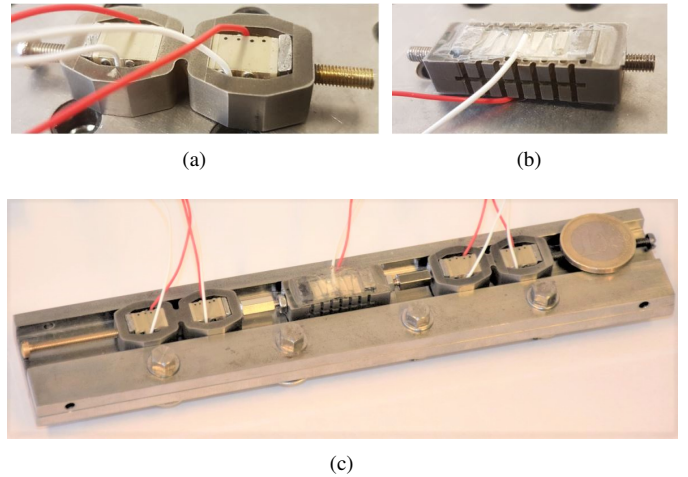


Figure 10: IM prototype, (a) CM, (b) EM and (C) assembly of different parts including PAs

##### 5.1. Noliac Piezo-actuator test off load

In this work, four NAC2021-H10, and one NAC2021-H16 are used in the CM and EM respectively. In order to validate the characteristics of NAC2021-H10 and NAC2021-H16, the free PAs are excited with DC Voltage of [20 40 60 80]V. The displacement in forward stroke has been measured using High-accuracy Laser displacement sensor (LK-G Series, KEYENCE). Fig.11 shows the displacement versus applied DC voltage. As expected, the measured displacement is proportional to the applied voltage. On the other hand, the characteristics given in Tab.2 considered at 80 V (determined by a linear relationship with those of 200 V) presented by the standard deviation are very close to the measured displacement. In addition, the four PAs in CM have practically the same behavior.

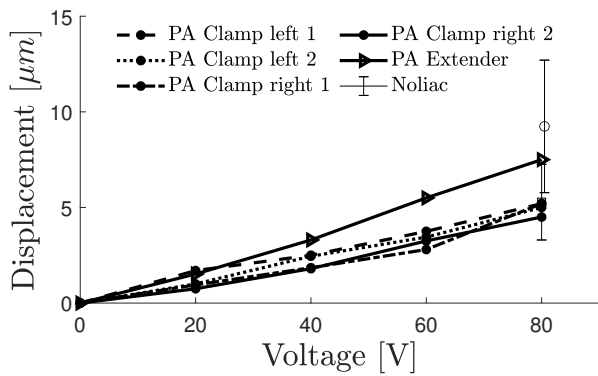


Figure 11: Free PAs displacement in forward stroke versus applied DC voltage

## 5.2. Calibration of the pre-stressing force

The PAs used in the development of the IM need to be calibrated for accurate system response. In order to balance the contribution of the four PAs of the two CMs for the same applied voltage, the pre-stressing force of the PAs must be the same. This allows both CMS to behave in the same manner. For this reason, a force sensor to measure this pre-stressing force has been designed.

### 5.2.1. Signal conditioning piezoelectric sensor

The force sensor is based on PA connected to charge amplifier that produces an output, which is a function of the electrical charge flowing into the input. The charge amplifier reported in Fig.12(a) acts as an integrator and continuously compensates

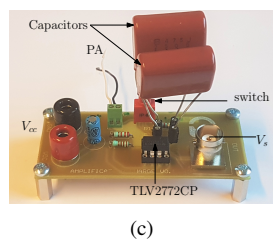
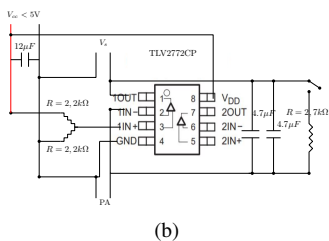
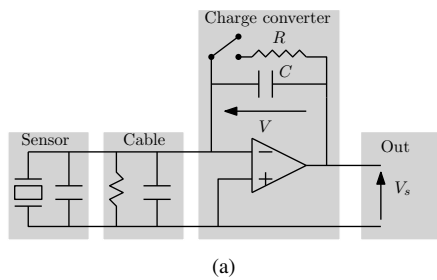


Figure 12: Designed PA charge amplifier, (a) basic Equivalent circuit for PA connected to charge amplifier (b) detailed equivalent circuit (c) practical implementation

the electric charge  $Q$  produced by the sensor through an equivalent charge. The charge amplifier therefore converts an input electric charge  $Q$  into an output proportional voltage  $V_s$  that can

be easily processed. The capacitance  $C$  determines the resolution and the maximum measured force, while the resistance  $R$  is used on one hand to determine the high-pass filter cut frequency and on the other hand to control the offset of the sensor through the switch. In this work a Texas Instruments TLV2772CP is used as amplifier, where the designed PA charge amplifier is given in Fig.12(b) and 12(c).

### 5.2.2. PA pre-stressing force sensor

The method for calibrating the PA pre-stress force is based on the charge amplifier and tensile-testing machine as shown in Fig.13. A pre-stress force was applied on the PA by a Compression Digital Hand Tester (CDHT). The charge amplifier converts the electrical charge to a voltage  $V_s$  through an oscilloscope. In order to calibrate the five PAs, different lev-

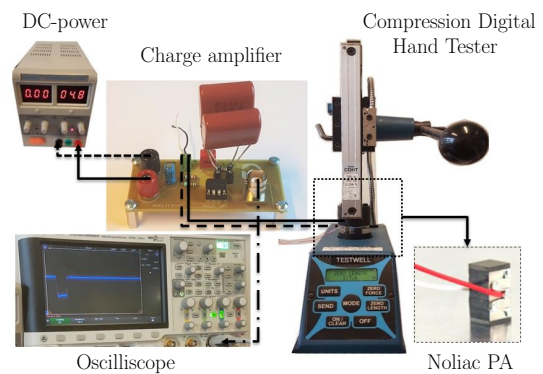


Figure 13: Experimental set-up used for the calibration of the PA pre-stress force

els of pre-stress force were applied for each PA as shown in Fig.14(a) for the PA in the extender (NAC2021-H16). The voltage is fixed to  $\frac{V_{cc}}{2}$ ; under no pre-stress force. When different pre-stressing forces were applied, the voltage is decreasing. It should be noted that the maximum pre-stress force can be measured near 0 voltage. This experiment was repeated for the four PA (NAC2021-H10) in the CMs and only one PA is presented in Fig.14(b). As can be seen, the results are different from that of NAC2021-H16 because the internal equivalent electrical capacitances of the PAs are different. For each measurement condition, and for each PA, the correlation between the pre-stressed force and the generated voltage signal is shown in Fig.14(c). The linear regression yields the force voltage relationship for the pre-stressed force sensor corresponding to [279, 258, 271, 269]  $N V^{-1}$  for the four NAC2021-H10 and [110]  $N V^{-1}$  for NAC2021-H16. Finally, as shown in Fig.14(d), the contribution of the four PAs in the two CM was calibrated and fixed to 75 N using the pre-tightening screws (see Fig.10(a) and 10(b)) instead of CDHT (Fig.13).

## 5.3. Extender and clamps displacement measurement

In this part, after calibration of pre stressing forces, the behaviour of CMS and EM according to Fig.6 and 7, will be validated independently with measurements. For this reason clamped-free boundary conditions have been imposed. The

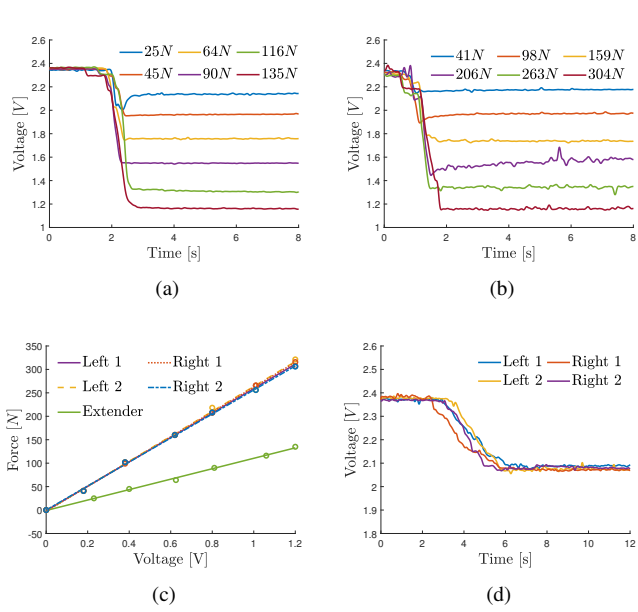


Figure 14: Calibration of the PA pre-stressing force (a) PA in the Extender, (b) PA in the CM, (c) PA Force voltage relationship in the EM and CM, (d) Calibration of the four PAs pre-stressing force in the two CMs

non-contact measurement laser displacement sensor (LK-G Series, KEYENCE) has been used for displacement measurement at different surfaces as indicated in Fig.15(a) and 16(a) for the EM and CM respectively. The PAs are excited with DC-voltage from 0 to 80 V according to forward and reverse scan directions. Fig.15(b) shows the relationship between the measured extender displacement and the applied voltage. It can be seen from the figure that when the voltage is applied to the PA, the forward displacement curve does not coincide with the reverse displacement curve. The maximum measured displacement at the end of the extender is  $5 \mu\text{m}$  at 80 V. Comparing the results obtained in experiments at 80 V (Fig.15(b)) with the previous computational results at 80 V (Fig.15(c)), it is possible to conclude that, the theoretical and practical results are very close. It should be noted that a pre-stressed force of 0.13 kN is applied to the extender and was taken into consideration in Fig.15(c). We have determined the force displacement characteristics by knowing the blocking force and the free displacement of the piezo-actuator at 200 V presented in Tab.2. The characteristics at 80 V are determined by a linear relationship with those of 200 V. Similarly, the same experiment was repeated in the case of left and right CM. The displacement was measured on five surfaces as indicated by Fig.16(a). As can be seen in Fig.16(b), 16(c) and 16(d), since the PAs and the pre-stressed force are identical, the CMs have the same behaviour. The displacement differences between the surfaces 2,3,4 and 5 ( $\delta=0.3 \mu\text{m}$ ) can be related to the asymmetry of the CMs structure because of the chosen tolerance ( $\pm 0.1 \text{ mm}$ ). In addition, the total displacement ratio between surfaces 1 and 2, for example, is similar to the theoretical results (Fig.6 and 7) and subsequently confirmed by Fig.16(e) for one activated PA. In Fig.16(e) we have presented the characteristics of the used PA in the CM at 200 V (black line) and at 80 V (black dashed line) according to Tab.2.

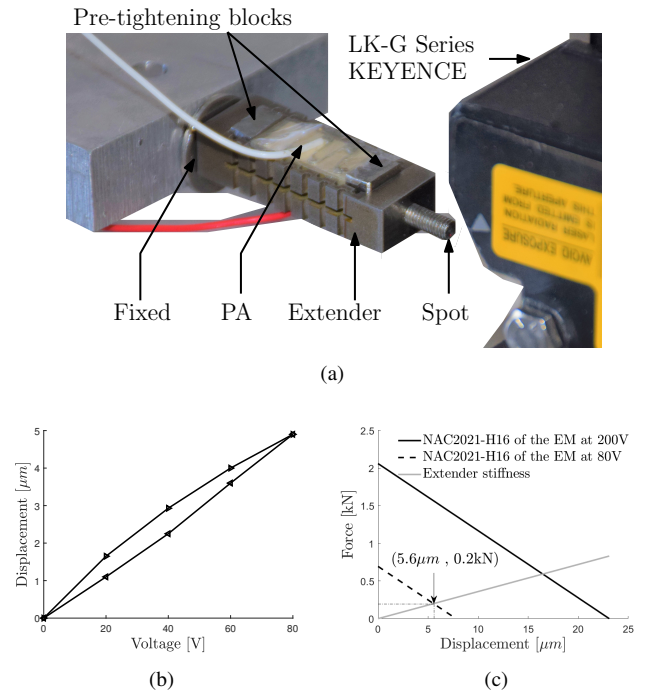


Figure 15: Extender displacement measurement, (a) Experiment setup, (b) Displacement versus applied voltage, (c) Force versus displacement output at 200 and 80 V.

The grey line represents the stiffness of the CM calculated from Fig.6. The intersection between CM stiffness and PA characteristics represents the working point in term of force and induced displacement. Here the applied pre-stressed force of 0.075 kN was taken into consideration. If 2 PAs of the left or right CM are considered i.e.  $2 \times 6.4 \mu\text{m}$  as a total displacement, then the simulation results (Fig.6(a)) are close to those of the measurement with a deviation of  $1 \mu\text{m}$  (Fig.16(a)). Regarding the mechanical hysteresis presented in Fig.15(b) and Fig.16(d), it is possible to use a feedback loop in order to compensate for this hysteresis and to ensure stability of the IM. Feedback signal can be position, force or dielectric charge. In addition, in most of these IMs the voltage is kept constant while the excitation frequency varies allowing its speed to be varied, which reduces the effect of hysteresis.

#### 5.4. Blocking force Measurement

In order to determine the imposed blocking force, a CDHT has been used as illustrated in Fig.17. The weight placed on the arm of the CDHT is used to stabilize the applied force and to obtain a predetermined normal force. In the first step, the CDHT applies a normal force (limited to 0.27 kN) on the moving rail through a rigid parallel metal mass in order to distribute forces evenly along the rail. In the second step, the clamping bolts are applied in order to keep the imposed force by CDHT. In order to determine the tangential force applied in practice, a measurement of the coefficient of friction between the rotor and the stator was carried out and detailed hereafter.

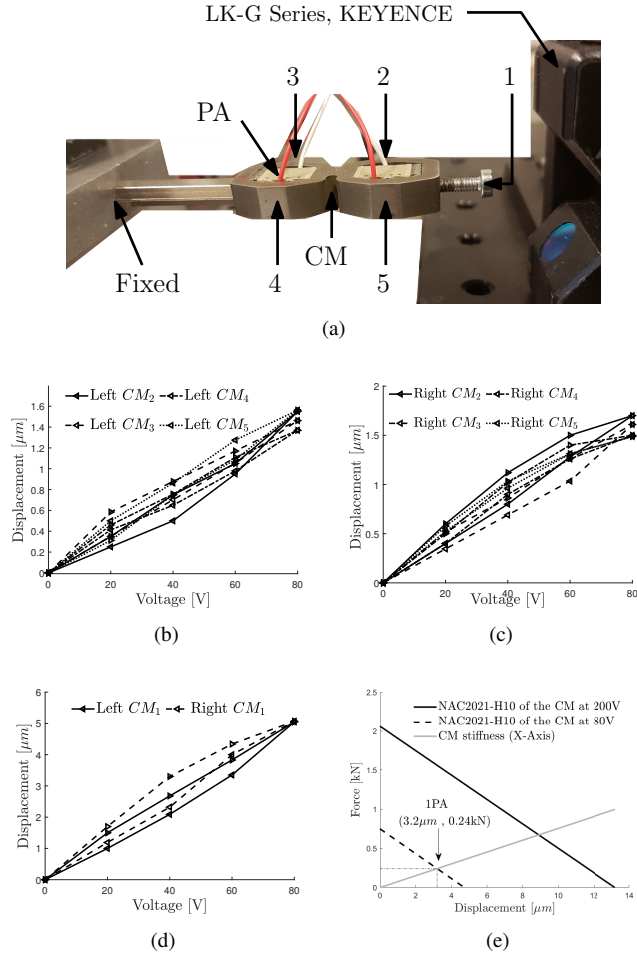


Figure 16: CMs displacement measurement, (a) Experiment setup, (b) Left CM displacement versus applied voltage, (c) Right CM displacement versus applied voltage, (d) Right and left CM displacement measurement at position 1, (e) Force versus displacement output at 200 and 80 V for one PA

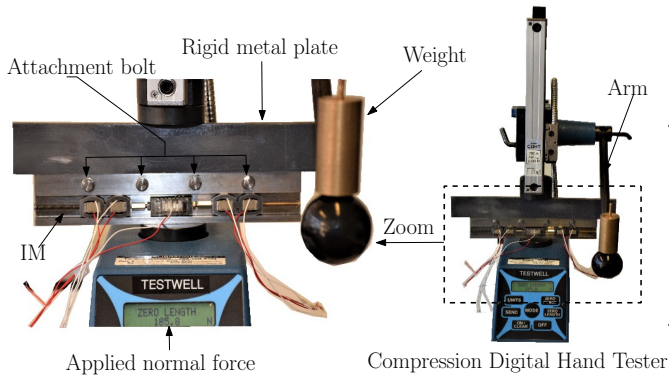


Figure 17: Experimental set-up, a CDHT applies a normal force on the moving rail, then fixed by attachment bolts

#### 5.4.1. Friction coefficient measurement

The developed experiment set-up presented in Fig.18(a) is capable of measuring the static coefficient of friction  $\mu$  between the rotor and stator. The idea is based on the developed PA force

430 sensor presented in subsection.5.2. Experiments were performed with an additional PA connected to a charge amplifier. A static force is applied on the additional PA, which is transmitted to the rotor through pre tightening block under different applied normal forces (125 N, 220 N 375 N) generated by CDHT. As

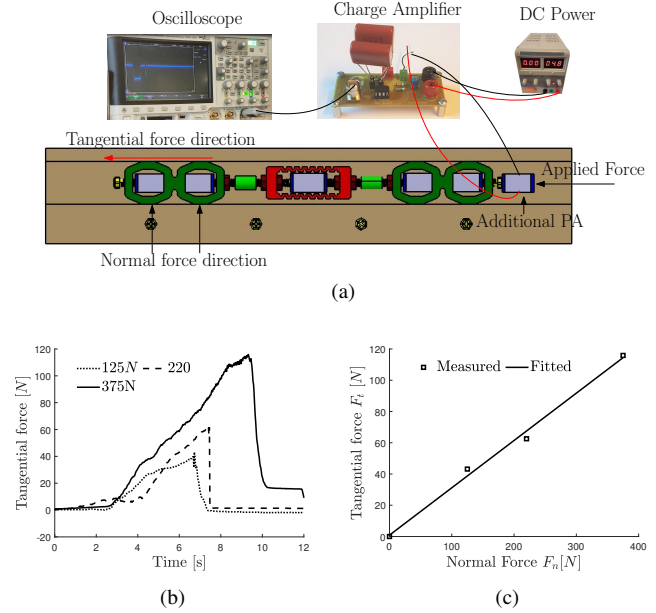


Figure 18: Static friction coefficient measurement, (a) Experiment set-up, (b) applied tangential force variation, (c) tangential force versus normal force

435 soon as the tangential force exceeds the maximum value of the static friction, the rotor begins to slide, driven by the applied force as shown in Fig.18(b). As can be seen, when the rotor is not moving, the rotor experiences static friction. The friction increases as the applied force increases until the rotor moves. After the rotor moves, no effort is transmitted to the rotor. It should be noted that, when the applied force is just equal to the force of static friction represented by the maximum tangential force, then the rotor is on the verge of slipping. Consequently the friction coefficient is measured when the tangential force is maximal as shown in Fig.18(c). The measured friction coefficient is  $0.31 \pm 0.03$ . For the rest of the work, the measured friction coefficient is taken into consideration in order to determine the tangential friction force.

#### 5.5. Low frequency power supply

445 In order to validate the performances of the IM in terms of speed and driving force, a power supply has been used to generate the excitation signals as presented in Fig.3(b). The equivalent circuit that has been used for IM operation is given in Fig.19. When one of the switches  $I_1$ ,  $I_2$ , or  $I_3$  is open, the corresponding PA ( $PA_{L1}$ / $PA_{L2}$ ,  $PA_E$ , or  $PA_{R1}$ / $PA_{R2}$ ) is operating. In the opposite case, we short-circuit the voltage generator and the PAs. The purpose of the short circuit is to return to the initial state, i.e. the initial size of the PAs. The three series resistors (R) are used to avoid too much current when the voltage generator is short-circuited. Therefore, it is possible to operate the switches to obtain the desired sequences. This power supply is

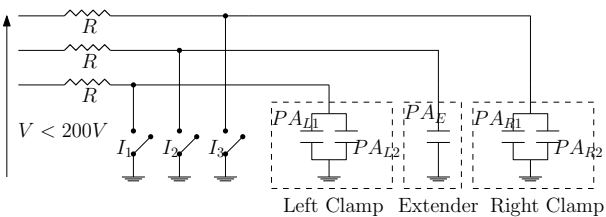


Figure 19: Low frequency power supply circuit of IM

designed for very low frequency, due to the lack of an L filter (a coil) at the input of the power supply. This coil must be chosen according to the excitation frequency in order to build a resonance with the internal capacitance of the piezo actuator. This makes it possible to control the rise and fall time of the three applied voltages.

### 5.6. Motor speed analysis at low frequency

In this part, a blocking force of 300 N was imposed according to section 5.2. Since the friction coefficient was measured (figure 19), a CDHT has been used as illustrated in Fig.20. Therefore, a normal force of 967 N was imposed and then we tightened the screws which hold the rotor to the stator. The IM is excited with three square signals at frequency of 0.25 Hz with voltage amplitude of 80 V. The displacement is measured on the left axial screw using a laser displacement sensor (LK-G Series, KEYENCE) as shown in Fig.20.

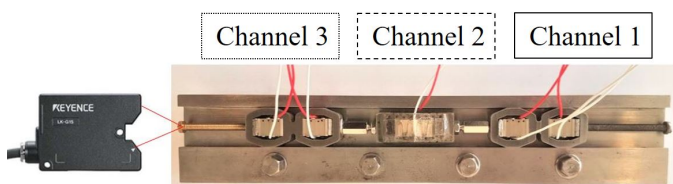


Figure 20: IM displacement measurement

The motion in both forward and backward directions is presented in Fig.21 and Fig.22 respectively. As expected when the motion sequence of the PAs in Channel 1 and channel 3 is permuted, a backward motion is obtained. As can be seen in Fig.21, when the PAs in the left CM are excited with voltage of channel 3 a displacement is measured (according to Fig.20.) in the axial direction and the corresponding clamp is open. In the second step, the PA in the extender is excited with channel 2 and the extender displacement is measured. At the second half period of channel 3, the right CM is turned "on" while the left CM is turned "off". Consequently, the left CM retracts and returns to its original state which justifies the decreased measured displacement (at  $t = 2s$  for each cycle). During this second half period, the displacement remains almost constant, because the displacement is measured on the left clamp which is closed. When the extender is turned off a slight decrease in displacement is noted. This, may be caused by some slipping occurring or by the retraction force which is greater than the blocking force. The same behavior is obtained for backward

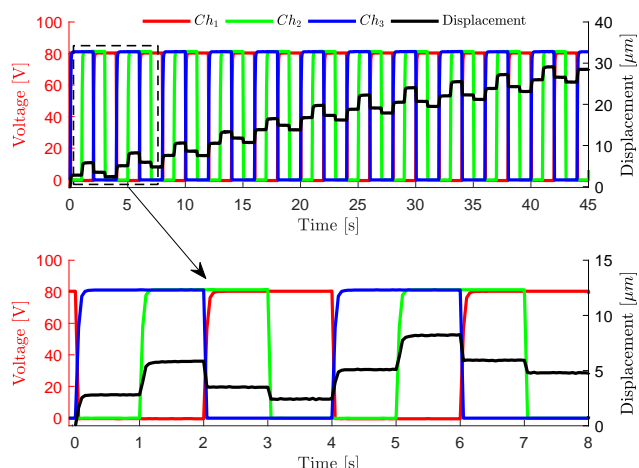


Figure 21: Motion sequence during (11 cycles Top, 2 cycles bottom) with induced displacement according to forward motion for an applied voltage of 80 V with frequency of 0.25 Hz

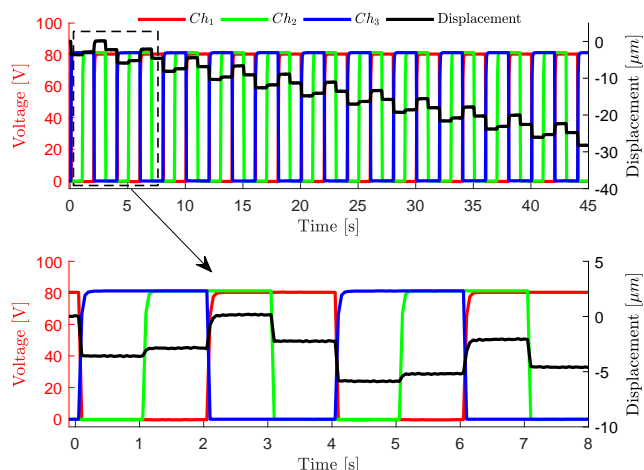


Figure 22: Motion sequence during (11 cycles Top, 2 cycles bottom) with induced displacement according to backward motion for an applied voltage of 80 V with frequency of 0.25 Hz

motion (Fig.22). After 10 cycles measured during 40 s, the average speed for the forward and backward motion at 0.25 Hz is  $0.57 \mu\text{m s}^{-1}$  and  $0.56 \mu\text{m s}^{-1}$  respectively.

The same experiment with the same conditions was repeated at different rails position, and the result reported in Fig.23 shows that, the measured displacement/cycle is influenced by the position of the motor through rails which is may be due to the chosen tolerance.

#### 5.6.1. Frequency influence

The speed of the IM is tested at different drive frequency while the applied voltage is 80 V. Fig.24 shows the obtained displacements curves at different excitation frequencies. With the increase of frequency, the total measured displacement is

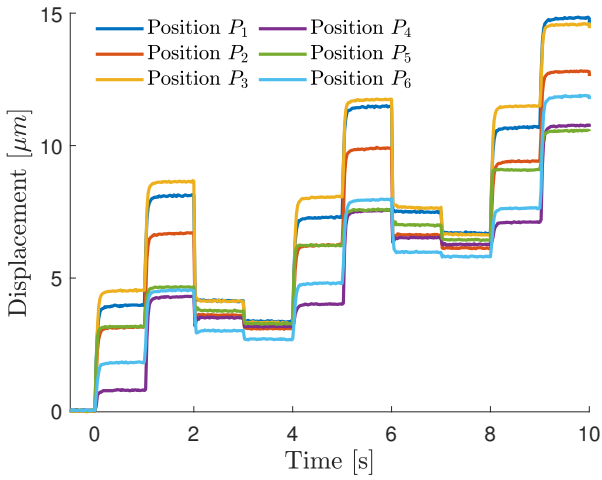


Figure 23: Measured displacement according to forward motion at different<sup>525</sup> position of the rail

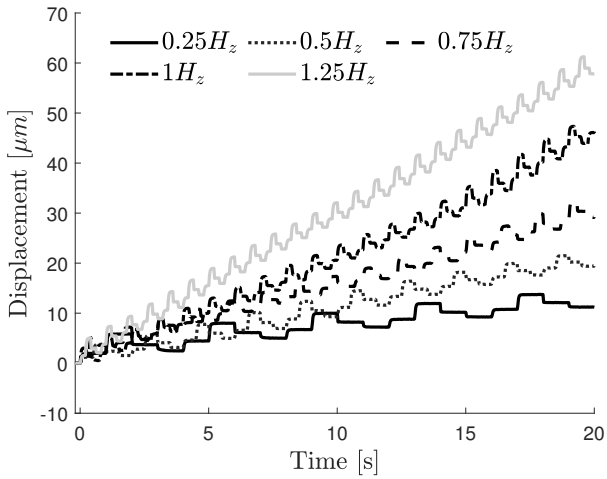


Figure 24: Output displacement of the IM measured on the clamping device vs frequency of input voltage of 80 V

510 increasing and shows good linearity with respect to the time, as confirmed by Fig.26 for the frequency-speed curve. The speed of the IM rises from  $0.57 \mu\text{m s}^{-1}$  at 0.25 Hz to  $2.9 \mu\text{m s}^{-1}$  at 1.25 Hz.

### 5.7. Load Influence

515 The experiment shown in Fig.25 was used to measure the speed of IM motor under load. A weight of 5 N was attached to the IM through cable and pulley. The IM is excited at different drive frequency with an applied voltage of 80 V and a friction<sup>535</sup> force of 300 N as described in section 5.6. Fig.26 shows that, the motor is able to push a load of 5 N with speed of  $0.8 \mu\text{m s}^{-1}$  measured at frequency of 1 Hz. Moreover, the velocity of the IM increases when increasing frequency. However it decreases in comparison with the IM speed without load. It should be<sup>540</sup>

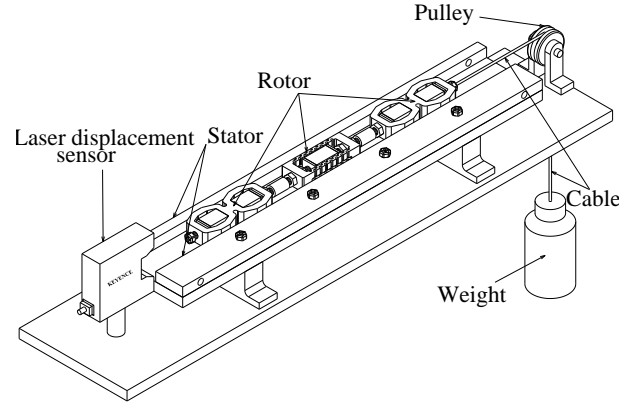


Figure 25: Experimental set-up under load with displacement measurement

noted that the weight is limited to 5 N because of inadequate power supply. As can be seen in Fig.21, when changing the role of the two clamps for example, the two curves  $Ch_1$  and  $Ch_3$  corresponding to the left and right CM intersect. This means that, both clamps are almost open at 40 V which limits the load capacity.

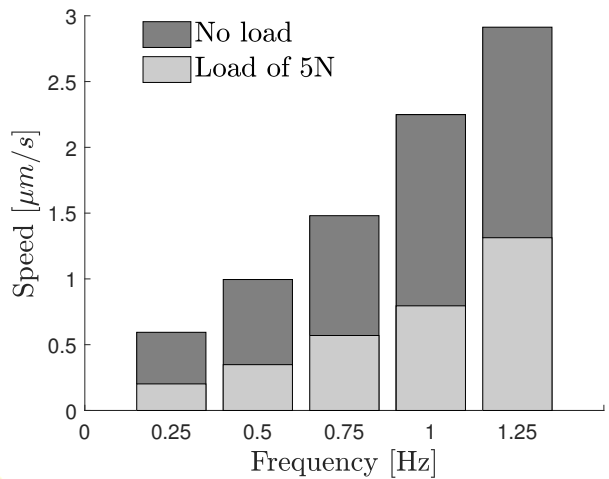


Figure 26: Measured speed with and without load for an applied voltage of 80 V

## 530 6. Discussion

The different parts of the IM were validated experimentally and independently (Fig.15(c) and Fig.16) while the used Noliac piezo-actuator largely met the specifications as shown in Fig.11. However, in the experiment, the clamping force of 300 N and driving force of 5 N are significantly different from the theoretical results. In fact, (300 N and 5 N) do not represent the maximum performances of the motor but rather the test conditions in order to validate the working principle of the motor presented in Fig.21 and Fig.22.

We have not tested the maximum performance of the motor

and this is due to the inadequacy of the used low frequency<sup>595</sup> power supply. In fact, the maximum input voltage of the motor is 200 V but the experiment was realized under 80 V (see Fig.21 and Fig.22). This means that only 40% of the maximum performances of the IM was used. On the other hand, another limitation is linked to the used compression digital hand tester (CDHT) which is limited to 2700 N. This means that technically we can apply a maximum clamping force of 840 N i.e.<sup>600</sup> (2700\*0.31 N). Concerning the driving force of 5 N, in the experiment as shown in Fig.21, the two clamps of the motor are excited by 180 degrees phased shifted ( $Ch_1$  and  $Ch_3$ ). This leads to the intersection of the two signals, i.e. at a given instant (for example at 2s) the two clamps are energized which means<sup>605</sup> that both clamps are practically open and therefore limits the load and the conditions test i.e. the clamping force should be higher than the driving force. Regarding the measured friction coefficient which does not correspond to the theoretical value, in order to ensure the high friction coefficient in the actual mechanism, as a solution, it is possible to change the nature<sup>610</sup> of the material of the rails (Aluminum for example) allowing the tangential friction to be increased more. Another alternative solution (a bit expensive) is to choose a similar Noliac piezo actuators but with section of  $10\text{ mm}^2 \times 10\text{ mm}^2$  corresponding<sup>615</sup> to a blocking force of 4200 N. Otherwise, regarding the drive electronics and the complexity of sequential circuits for the presented IM with 5 piezo actuators, since the piezo actuators of the blocking system are similar and excited in a parallel way (see Fig.20) this should not generate a degree of complexity<sup>620</sup> with regard to IM with 3 piezoelectric actuators.

## 7. Features and advantages of the proposed IM

As presented by the state of the art, the load capacity of<sup>625</sup> these linear motors remains limited. The highest force of these motors was obtained in a recent work [25] by combining the inchworm and stick-slip driving principles with a complicated clamping mechanism (ball-screw-based) resulting in a consequent volume of  $112\text{ cm}^3$ . Compared to [25], the proposed IM is 10 times smaller even if 5 PAs are used without adding a degree of complexity in the electrical excitation. The design of the proposed IM is simple and flexible. The introduction of doubled clamping mechanism makes the proposed IM rigid to support high clamping force but also sufficient to introduce more PAs in a compact size. Moreover, since 8 contact areas are considered instead of 4 in traditional design [22], the parallelism of the guide rails on both sides is improved. As confirmed by the literature most of these IM require electrical excitation to<sup>635</sup> hold the rotor in a fixed position. The presented motor has advantages in terms of energy consumption, with respect to low-power IM that does not require power when holding a position. With regard to certain applications where blocking and driving<sup>640</sup> forces, weight, volume and energy consumption must be taken into consideration, the proposed motor is suitable. For example, in terms of ideal IM maximum output, it can be used to adjust aircraft seats position. For this application, a high block-<sup>645</sup>ing force is necessary to withstand the forces related to take-off

and landing but also the shock forces. In terms of testing conditions, this motor is suitable for precision positioning systems [32] particularly on the vertical axis for holding a position.

## 8. Conclusion

This work proposed design and experimental analysis of a compact piezoelectric IM that ensures full clamping ability when not electrically activated (self-locking at rest). The design, manufacture and motor assembly are simple with a very compact size (motor weight of 100 g and volume of  $11.5\text{ cm}^3$ ). Through FEA, this paper has addressed how the CM and EM are designed, and how the appropriate PAs were chosen. The working principle of the IM was analyzed and verified, and the feasibility of the motor was verified through experiments. The friction force between the rotor and the stator was estimated through friction coefficient measurement and a method to balance the contribution of the two doubled CMs based on pre-stressing force calibration was proposed. By using a preliminary power supply limited to 80 V, presenting 40% of the maximum input voltage of the used PAs, a driving force of 5 N and a clamping force of 300 N were measured. The motion principle of IM was tested along the two directions with a measured speed of  $2.25\text{ }\mu\text{m s}^{-1}$  at frequency of 1 Hz.

Future work includes development of high frequency power supply including a phase shift between voltage of  $Ch_1$  and  $Ch_3$  i.e  $Ch_3$  should start after the voltage of  $Ch_1$  returns to 0. Secondly, closed loop control of IM position will be implemented [33]. Thirdly, the mechanical structure is brought into contact and friction between stator and rotor, one of which moves relative to the other and consequently leads to piezo-motor wear. knowing the ageing effect, temperature effect [34] and the duration of its lifetime like that of the piezo-actuators (more than  $10^{10}$  cycles) is an important point.

## Acknowledgment

This work is generated in the context of the project PASATS, a partnership between CentraleSupélec, Faurecia and CSIR-India, funded by the IFPCPAR (Indo-French Centre for the Promotion of Advanced Research) under the grant number IFC/7123. It also received direct support from the company Faurecia.

## References

- [1] B. Zhang, Z.Zhu, Design of an inchworm-type linear piezomotor, SSIS, 1994, vol. 2190, pp. 528-540 doi: 10.1117/12.175214
- [2] T. Galante, et al, Design, Modeling, and Performance of a High Force Piezoelectric Inchworm Motor, Journal of Intelligent Material Systems and Structures, vol. 10, no. 12, pp. 962-972, Dec. 1999. doi:10.1106/21LN-RUY-35CH-C1FD
- [3] J. Park, et al Development of a compact displacement accumulation actuator device for both large force and large displacement, Sensors and Actuators A: Physical, vol. 90, no. 3, pp. 191-202, May 2001. doi:10.1016/S0924-4247(01)00521-0
- [4] M. Vaughan and D. J. Leo, Integrated Piezoelectric Linear Motor for Vehicle Applications, pp. 113-121, Jan. 2002. doi: 10.1115/IMECE2002-32942.

- [5] N. Cho, and W. Jang, The Design and Characterization of a Piezo-Driven Inchworm Linear Motor with a Reduction-Lever Mechanism, *JSME International Journal Series C Mechanical Systems, Machine* 20 Elements and Manufacturing, vol. 47, no. 3, pp. 803–811, 2004. doi:10.1299/jsmec.47.803.
- [6] Qin Xu, et al. Electromechanical translation apparatus US 20050035687 A1, 04-March-2003.
- [7] P. E. Tenzer and R. B. Mrad, A systematic procedure for the design of piezoelectric inchworm precision positioners, *IEEE/ASME Transactions on Mechatronics*, vol. 9, no. 2, pp. 427–435, Jun. 2004. doi: 10.1109/TMECH.2004.828627.
- [8] G. Powers et al, High-power Inchworm actuators for extended-range precision positioning, *Proceedings of SPIE 2005*, 5762, 278–298. doi:10.1117/12.600584.
- [9] J. Li, et al, Design and development of a new piezoelectric linear Inchworm actuator, *Mechatronics*, vol. 15, no. 6, pp. 651–681, 2005. doi: 10.1016/j.mechatronics.2005.02.002.
- [10] C. Moon, et al, A new fast inchworm type actuator with the robust I/Q heterodyne interferometer feedback, *Mechatronics*, vol. 16, no. 2, pp. 105–110, Mar. 2006. doi: 10.1016/j.mechatronics.2005.10.003.
- [11] S. P. Salisbury, R. B. Mrad, D. F. Waechter and S. E. Prasad, "Characterization of a Piezoworm Stage," 2007 IEEE/ASME international conference on advanced intelligent mechatronics, 2007, pp. 1–5. doi:10.1109/AIM.2007.4412444.
- [12] L. Ma, C. Jiang, J. Xiao, K. Wang, W. Xie and B. Liu, "A piezoelectric inchworm actuator based on the principle of flexible amplification," 2013 International Conference on Manipulation, Manufacturing and Measurement on the Nanoscale, 2013, pp. 201–206. doi: 10.1109/3M-NANO.2013.6737414.
- [13] E. Williams, et al, Design of a large-force piezoelectric Inchworm motor with a force duplicator, *RobMech*, 2013, pp. 46–51. doi: 10.1109/RoboMech.2013.6685490.
- [14] Y. Liu, J. Yan, D. Xu, W. Chen, X. Yang, X. Tian, An I-shape linear piezoelectric actuator using resonant type longitudinal vibration transducers, *Mechatronics*, vol. 40, pp. 87–95, Dec. 2016. doi: 10.1016/j.mechatronics.2016.09.002.
- [15] M. Sun, et al, Research on a novel non-resonant piezoelectric linear motor with lever amplification mechanism, *Sensors and Actuators A: Physical*, vol. 261, no. Supplement C, pp. 302–310, Jul. 2017. doi: 10.1016/j.sna.2017.04.030.
- [16] Q. Pan et al., "Design, simulation, and motion characteristics of a novel impact piezoelectric actuator using double stators," *Smart Mater. Struct.*, vol. 31, no. 7, p. 075012, Jun. 2022, doi: 10.1088/1361-665X/ac736e.
- [17] X. Tian, Q. Quan, L. Wang, and Q. Su, An Inchworm Type Piezoelectric Actuator Working in Resonant State, *IEEE Access*, vol. 6, pp. 18975–18983, 2018. doi: 10.1109/ACCESS.2018.2814010.
- [18] M. Tahmasebipour and M. Sangchap, "A novel high performance integrated two-axis inchworm piezoelectric motor," *Smart Mater. Struct.*, vol. 29, no. 1, p. 015034, Dec. 2019, doi: 10.1088/1361-665X/ab545e.
- [19] L. He et al., "Resonant-type piezoelectric linear motor driven by harmonic synthesized mechanical square wave," *Review of Scientific Instruments*, vol. 91, no. 3, p. 035005, Mar. 2020, doi: 10.1063/1.5110774.
- [20] C. Li et al., "Development of a high-resolution, high-speed impact piezoelectric actuator using cross-frequency band method," *Smart Mater. Struct.*, vol. 31, no. 5, p. 055005, Mar. 2022, doi: 10.1088/1361-665X/ac5beb.
- [21] L. Wang, Y. Guan, Y. Liu, J. Deng and J. Liu, "A Compact Cantilever-Type Ultrasonic Motor With Nanometer Resolution: Design and Performance Evaluation," in *IEEE Transactions on Industrial Electronics*, vol. 68, no. 1, pp. 734–743, Jan. 2021, doi: 10.1109/TIE.2020.2965481.
- [22] H. Dong, T. Li, Z. Wang, and Y. Ning, "Design and experiment of a piezoelectric actuator based on inchworm working principle," *Sensors and Actuators A: Physical*, vol. 306, p. 111950, May 2020, doi: 10.1016/j.sna.2020.111950.
- [23] J. Cai, F. Chen, S. Lining, W. Dong. Design of a linear walking stage based on two types of piezoelectric actuators. *Sensors and Actuators A: Physical*, 2021, vol. 332, p. 112067.
- [24] TIAN, Yanling, HUO, Zhichen, WANG, Fujun, et al. A novel friction-actuated 2-DOF high precision positioning stage with hybrid decoupling structure. *Mechanism and Machine Theory*, 2022, vol. 167, p. 104511.
- [25] S. Shubao, S. Siyang, S. Yan, X. Minglong. Long-range piezoelectric actuator with large load capacity using inchworm and stick-slip driving principles. *Precision Engineering*, 2022, vol. 75, p. 167–179.
- [26] P. E. Tenzer and R. Ben Mrad, On amplification in inchworm precision positioners, *Mechatronics*, vol. 14, no. 5, pp. 515–531, Jun. 2004. doi: 10.1016/j.mechatronics.2003.10.004.
- [27] J. Ni and Z. Zhu, Design of a linear piezomotor with ultra-high stiffness and nanoprecision, *IEEE/ASME Transactions on Mechatronics*, vol. 5, no. 4, pp. 441–443, Dec. 2000. doi: 10.1109/3516.891056.
- [28] M. Sangchap, M. Tahmasebipour, and Y. Tahmasebipour, "A Linear Inchworm Piezomotor with a New Configuration: Design Considerations, Fabrication and Characterization," *Iran J Sci Technol Trans Mech Eng*, vol. 46, no. 1, pp. 149–160, Mar. 2022, doi: 10.1007/s40997-020-00409-x.
- [29] C. Yang, Y. Wang, and W. Fan, "Long Stroke Design of Piezoelectric Walking Actuator for Wafer Probe Station," *Micromachines (Basel)*, vol. 13, no. 3, p. 412, Mar. 2022, doi: 10.3390/mi13030412.
- [30] C. Giraud-Audine and F. Giraud, Preliminary feasibility study of a speed estimator for piezoelectric actuators used in forging processes, in *Proceedings of the 2011-14th European Conference on Power Electronics and Applications (EPE 2011)*, 2011, pp. 1–10.
- [31] F. Claeysen, et al, Piezoactive actuator with dampened amplified movement, US6927528B2, 09-Aug-2005.
- [32] J. Li, H. Huang, and T. Morita, "Stepping piezoelectric actuators with large working stroke for nano-positioning systems: A review," *Sensors and Actuators A: Physical*, vol. 292, pp. 39–51, Jun. 2019, doi: 10.1016/j.sna.2019.04.006.
- [33] S. Ghenna, F. Giraud, C. Giraud-Audine, and M. Amberg, "Vector Control of Piezoelectric Transducers and Ultrasonic Actuators," *IEEE Transactions on Industrial Electronics*, vol. 65, no. 6, pp. 4880–4888, Jun. 2018, doi: 10.1109/TIE.2017.2784350.
- [34] H. Dong, T. Li, Z. Wang, and Y. Ning, "Numerical calculation of inchworm actuator reliability: effect of space temperature and material parameters," *Aircraft Engineering and Aerospace Technology*, vol. ahead-of-print, no. ahead-of-print, Jan. 2022, doi: 10.1108/AEAT-01-2022-0006.

750

755

760

765



**Sofiane Ghenna** received the Engineer's degree in Electrical Engineering in 2011 from National Polytechnic School of Algiers, Algeria and the Master's degree in Electrical Engineering Systems from National Polytechnic Institute - ENSEEIHT Toulouse, France, in 2012 and the Ph.D degree in electrical engineering from Lille University, France, in 2016. After one year as Temporary Teaching and Research Assistant

at Lille University, and two years as Post-Doctoral researcher at CentraleSupélec, Paris, France, he is currently Associate Professor at Université Polytechnique Hauts-de-France Valenciennes, France. His research interests include design, modeling and control of smart materials based actuators.

770

775



**Yves Bernard** was born in Paris, France, on January 8, 1974. He received the diploma degree in energy transformation from the University of Paris-Sud Orsay, Paris, and the doctoral degree in magnetic hysteresis modeling in the finite element modeling method from the University of Paris-Sud Orsay, in 2000.

He has been a Professor with the University of Paris-Sud Orsay, since September 2012. His research interests include modeling and conception of piezoelectric devices.

780

785



**Laurent Daniel** received the Ph.D. degree from the École Normale Supérieure de Cachan, Cachan, France, in 2003 and the Habilitation degree in Physics from the Université Paris-Sud, Orsay, France, in 2011. Since 2015, he has been a Full Professor with CentraleSupélec, Université Paris-Saclay, Gif-sur-Yvette, France. His research activities, within the Group of Electrical Engineering of

Paris (GeePs), are dedicated to electromechanical and magnetomechanical couplings in materials for electrical engineering applications. He is notably involved in the definition of multiscale methods for the prediction of such coupled phenomena and in the development of dedicated experimental characterization setups. Since 2014, he has been the Director of the Automotive Mechatronics Chair, a partnership between CentraleSupélec, Esigelec and the automotive company Faurecia.

795